

Flight control for air-breathing hypersonic vehicles using linear quadratic regulator design based on stochastic robustness analysis^{*}

Lin CAO¹, Shuo TANG¹, Dong ZHANG^{†‡2}

(¹College of Astronautics, Northwestern Polytechnical University, Xi'an 710072, China)

(²Shaanxi Aerospace Flight Vehicle Design Key Laboratory, Xi'an 710072, China)

[†]E-mail: zhangdong@nwpu.edu.cn

Received June 25, 2016; Revision accepted Oct. 14, 2016; Crosschecked July 12, 2017

Abstract: The flight dynamics model of air-breathing hypersonic vehicles (AHVs) is highly nonlinear and multivariable coupling, and includes inertial uncertainties and external disturbances that require strong, robust, and high-accuracy controllers. In this paper, we propose a linear-quadratic regulator (LQR) design method based on stochastic robustness analysis for the longitudinal dynamics of AHVs. First, input/output feedback linearization is used to design LQRs. Second, subject to various system parameter uncertainties, system robustness is characterized by the probability of stability and desired performance. Then, the mapping relationship between system robustness and LQR parameters is established. Particularly, to maximize system robustness, a novel hybrid particle swarm optimization algorithm is proposed to search for the optimal LQR parameters. During the search iteration, a Chernoff bound algorithm is applied to determine the finite sample size of Monte Carlo evaluation with the given probability levels. Finally, simulation results show that the optimization algorithm can effectively find the optimal solution to the LQR parameters.

Key words: Air-breathing hypersonic vehicles (AHVs); Stochastic robustness analysis; Linear-quadratic regulator (LQR); Particle swarm optimization (PSO); Improved hybrid PSO algorithm

<http://dx.doi.org/10.1631/FITEE.1601363>

CLC number: TP27; V24

1 Introduction

Air-breathing hypersonic vehicles (AHVs) have attracted a lot of attention for decades because of their prospects for high-speed, large payload transportation and excellent cost effectiveness to access the space routine. The flight control system plays an important role in making AHVs feasible and efficient (Fidan *et al.*, 2003; Rodriguez *et al.*, 2008). Although there have been numerous efforts on this issue, designing a flight control system for AHVs is still a challenge. Due to its high flight speed, the vehicle is sensitive to

the changes in flight conditions, which results in difficulties in measuring and estimating the aerodynamic properties (Bolender and Doman, 2005). In addition, the requirements of flight stability and high-speed response, strong couplings, and various random uncertainties make it more difficult (Williams *et al.*, 2006; Bolender *et al.*, 2007). Much research has been conducted on the design of AHV controllers, and a comprehensive review of hypersonic flight dynamics and control approaches was given in Xu and Shi (2015). Linear control approaches were applied for AHV flight control, e.g., the linear-quadratic regulator (LQR) method (Grove *et al.*, 2005; Wang and Stengel, 2013) and gain-scheduling method (Arun Kishore *et al.*, 2008; Ge *et al.*, 2011). The linear controller was designed around the specified trim condition by linearizing the nonlinear longitudinal

[‡] Corresponding author

^{*} Project supported by the National Natural Science Foundation of China (No. 11672235)

 ORCID: Lin CAO, <http://orcid.org/0000-0002-8943-9479>

© Zhejiang University and Springer-Verlag Berlin Heidelberg 2017

dynamics. Use of the linearized model indicates that the linear control method cannot reflect the nonlinear characteristics of AHVs. In recent years, nonlinear techniques have been widely used in AHV control, such as feedback linearization (Dickeson *et al.*, 2009; Preller and Smart, 2015), back-stepping technique (Xu *et al.*, 2016), sliding-mode control (Xu *et al.*, 2004; Zong *et al.*, 2013), and intelligent control technique (Xu *et al.*, 2015a; 2015b; Xu and Zhang, 2015). Considering the random parametric uncertainties, strong inertial couplings, and unmodeled dynamics, the robust control technique is a feasible approach for AHV flight control design (Kuipers *et al.*, 2008; Rehman *et al.*, 2013; Pu *et al.*, 2014). As a robust control technique, robust control based on stochastic robustness analysis (SRA) was first demonstrated by Stengel and Ryan (1989; 1991) for the analysis of a linear control system. In the past few years, a lot of investigation has been done to make SRA possible for control system design. In Marrison and Stengel (1997) and Wang and Stengel (2001; 2002), SRA was employed to design the compensator for a benchmark problem to achieve a tradeoff between system stability and performance. Attempts have been made to apply robust control based on SRA to the control system design of hypersonic aircraft (Marrison and Stengel, 1998; Wang and Stengel, 2000) and general aircraft (Ray and Stengel, 1990). These studies have provided a practical systemic process for aircraft control design with linear/nonlinear synthesis and achieved good performance for the given control structures.

However, the aforementioned studies on SRA focused mainly on robustness measurement and analysis, and gave little attention to stochastic evaluation and optimization algorithms. The key point of stochastic evaluation is to make certain that the estimate provided by the stochastic algorithm is within a prior specified accuracy ζ from the true value, and with a high confidence $1-\mu$. In other words, the algorithm may fail to return an approximately correct estimate with a probability of at most μ (Piccoli *et al.*, 2009). Therefore, a suitable number of stochastic samples can not only correspond to the desired probabilistic levels, but also avoid involving a large number of unnecessary stochastic samples. Furthermore, the selection of the optimization algorithm is correlated strongly with the calculation efficiency.

An efficient optimization algorithm can reduce the computation complexity and quickly find the optimal solution.

Considering the two important factors mentioned previously (ζ and μ), we propose an improved LQR design method based on SRA for an AHV with assumed system parameter uncertainties and a large span of design parameter space. The proposed method employs SRA to characterize system robustness, and establishes a direct relationship between the design requirements and design parameters. Then, a novel hybrid particle swarm optimization (PSO) algorithm is used to maximize system robustness, which guarantees a successful tradeoff between system stability and system performance. The search ability and robustness of the proposed algorithm are verified by three nonlinear benchmark functions. During the search iteration, a Chernoff bound algorithm is applied to determine the finite sample size for Monte Carlo evaluation (MCE), which guarantees the estimated accuracy and confidence of stochastic evaluation. Finally, simulation results show the effectiveness and robustness of the proposed method in the AHV flight control application. The notations of this study are listed in Table 1.

Table 1 Variables and parameters of concern

Parameter	Description
V (ft/s)	Velocity
γ (rad)	Flight-path angle
h (ft)	Altitude
α (rad)	Angle of attack
q (rad/s)	Pitch rate
ϕ	Throttle setting
m (slug)	Mass
I_y (slug·ft ²)	Inertial moment
ρ (slug/ft ³)	Density of air
s (ft ²)	Reference area
\bar{c} (ft)	Mean aerodynamic chord
R_e (ft)	Radius of the Earth
r (ft)	Radial distance
T (lbf)	Thrust
L (lbf)	Lift
D (lbf)	Drag
M_y (slug·ft)	Pitching moment
C_T	Thrust coefficient
C_L	Lift coefficient
C_D	Drag efficient
M_a	Mach number

2 Mathematical model of an AHV

The longitudinal dynamics equations of an AHV were presented in Wang and Stengel (2000) and Parker *et al.* (2007). The equations of motion include an inverse-square-law gravitational model and centripetal acceleration for the nonrotating Earth. By normalizing the span of the vehicle to unit depth, the mathematical model of longitudinal dynamics is written in the stability axes as follows:

$$\dot{V} = \frac{T \cos \alpha - D}{m} - \frac{\mu \sin \gamma}{r^2}, \quad (1)$$

$$\dot{\gamma} = \frac{T \sin \alpha + L}{mV} - \frac{(\mu - V^2 r) \cos \gamma}{Vr^2}, \quad (2)$$

$$h = V \sin \gamma, \quad (3)$$

$$\dot{\alpha} = q - \dot{\gamma}, \quad (4)$$

$$\dot{q} = \frac{M_y}{I_y}, \quad (5)$$

where

$$L = \frac{1}{2} \rho V^2 S C_L, \quad (6)$$

$$D = \frac{1}{2} \rho V^2 S C_D, \quad (7)$$

$$T = \frac{1}{2} \rho V^2 S C_T, \quad (8)$$

$$M_y = \frac{1}{2} \rho V^2 S \bar{c} [C_M(\alpha) + C_M(\delta_e) + C_M(q)], \quad (9)$$

$$r = h + R_e. \quad (10)$$

The engine dynamics are assumed to take a second-order form as (Xu *et al.*, 2004)

$$\ddot{\phi} = -2\zeta\omega_n\dot{\phi} - \omega_n^2\phi + \omega_n^2\phi_c. \quad (11)$$

In this study, relative functions are used to approximate the aerodynamic coefficients around the nominal cruising condition. The nominal flight of the vehicle is at a trim cruise condition, i.e., $M_a=15$, $V=15\ 060$ ft/s, $\gamma=0^\circ$, $h=110\ 000$ ft, and $q=0^\circ$ /s. All of the parametric uncertainties are considered as an additive variance to the nominal values for control design. For illustration, the uncertain parameters are considered

as follows:

$$C_L(\alpha) = C_L^\alpha \alpha + C_L^0, \quad (12)$$

$$C_D(\alpha) = C_D^{\alpha^2} \alpha^2 + C_D^\alpha \alpha + C_D^0, \quad (13)$$

$$C_T(\phi) = C_T^\phi \phi + C_T^0, \quad (14)$$

$$C_M(\alpha) = C_{M_1}^{\alpha^2} \alpha^2 + C_{M_1}^\alpha \alpha + C_{M_1}^0, \quad (15)$$

$$C_M(q) = \frac{\bar{c}}{2V} q (C_{M_2}^{\alpha^2} \alpha^2 + C_{M_2}^\alpha \alpha + C_{M_2}^0), \quad (16)$$

$$C_M(\delta_e) = c_e(\delta_e - \alpha), \quad (17)$$

$$m = m_0(1 + \Delta m), \quad (18)$$

$$I_y = I_0(1 + \Delta I), \quad (19)$$

$$S = S_0(1 + \Delta S), \quad (20)$$

$$\bar{c} = \bar{c}_0(1 + \Delta \bar{c}), \quad (21)$$

$$\rho = \rho_0(1 + \Delta \rho), \quad (22)$$

$$c_e = c_{e0}(1 + \Delta c_e), \quad (23)$$

$$C_{M_1}^\alpha = C_{M_{10}}^\alpha (1 + \Delta C_{M_1}^\alpha). \quad (24)$$

The nominal parameters for control design are $m_0=9375$, $I_0=7 \times 10^6$, $S_0=3603$, $\bar{c}_0=80$, and $\rho_0=0.24325 \times 10^{-4}$. Readers can find details for the unvalued coefficients of the mathematical expressions above in Bolender and Doman (2005). The throttle setting ϕ_c and elevator deflection δ_e are the control inputs. The reference command of velocity and altitude are denoted as $V_d(t)$ and $h_d(t)$, respectively.

3 Tracking controller design

3.1 Input/output feedback linearization

Input/output feedback linearization is an effective approach for nonlinear system control. The objective is to transform the nonlinear system into a linear form by full-state feedback when satisfying the relative degree condition. Then, the classical linear system theory can be used for controller design synthesis.

Define $\mathbf{x}=[V, \gamma, h, \alpha, q, \phi, \dot{\phi}]^T$. The longitudinal dynamics of the AHVs described in Eqs. (1)–(5) can be considered as a standard form of a general multi-input multi-output nonlinear system:

$$\begin{aligned} \dot{\mathbf{x}}(t) &= \mathbf{F}(\mathbf{x}) + \mathbf{G}(\mathbf{x})\mathbf{u} \\ &= [f_1(\mathbf{x}), f_2(\mathbf{x}), \dots, f_n(\mathbf{x})]^T + \sum_{i=1}^m g_i(\mathbf{x}) \cdot u_i(\mathbf{x}), \end{aligned} \quad (25)$$

$$\mathbf{y} = \mathbf{H}(\mathbf{x}) = [h_1(\mathbf{x}), h_2(\mathbf{x}), \dots, h_m(\mathbf{x})]^T, \quad (26)$$

where $\mathbf{F} \in \mathbb{R}^n$, $\mathbf{G} \in \mathbb{R}^{n \times m}$, and $\mathbf{H} \in \mathbb{R}^m$ are sufficiently smooth functions. Each of the output channels is differentiated enough times to make the control inputs appear in the final expression. Assuming the system relative degree is well defined, the target of linearization is to obtain the resulting equations as

$$y_i^{(r_i)} = L_f^{r_i}(h_i(\mathbf{x})) + \sum_{j=1}^m L_{g_j} [L_f^{r_i-1}(h_i(\mathbf{x}))u_j], \quad (27)$$

where the Lie derivatives are defined as

$$\begin{aligned} L_f(h_i(\mathbf{x})) &= \frac{\partial h_i(\mathbf{x})}{\partial x_1} f_1(\mathbf{x}) + \frac{\partial h_i(\mathbf{x})}{\partial x_2} f_2(\mathbf{x}) + \dots \\ &\quad + \frac{\partial h_i(\mathbf{x})}{\partial x_n} f_n(\mathbf{x}), \\ L_f(h_i(\mathbf{x})) &= L_f[L_f^{-1}(h_i(\mathbf{x}))], \\ L_{g_j}(h_i(\mathbf{x})) &= \frac{\partial h_i(\mathbf{x})}{\partial \mathbf{x}} g_j(\mathbf{x}). \end{aligned}$$

When the described method is applied to the longitudinal dynamics of the hypersonic flight vehicle, the output dynamics for velocity V and altitude h can be acquired by differentiating V three times and h four times, i.e.,

$$\dot{V} = f_1(\mathbf{x}), \quad \ddot{V} = \omega_1 \dot{\mathbf{x}}, \quad \dddot{V} = \omega_1 \ddot{\mathbf{x}} + \dot{\mathbf{x}}^T \Omega_1 \dot{\mathbf{x}}, \quad (28)$$

$$\dot{h} = f_2(\mathbf{x}), \quad \ddot{h} = \omega_2 \dot{\mathbf{x}}, \quad \dddot{h} = \omega_2 \ddot{\mathbf{x}} + \dot{\mathbf{x}}^T \Omega_2 \dot{\mathbf{x}}, \quad (29)$$

$$\begin{cases} \dot{h} = f_3(\mathbf{x}), & \ddot{h} = \dot{V} \sin \gamma + V \dot{\gamma} \cos \gamma, \\ \ddot{h} = \ddot{V} \sin \gamma + 2\dot{V} \dot{\gamma} \cos \gamma - V \dot{\gamma}^2 \sin \gamma + V \ddot{\gamma} \cos \gamma, \\ h^{(4)} = \ddot{V} \sin \gamma + 3\dot{V} \dot{\gamma} \cos \gamma - 3V \dot{\gamma}^2 \sin \gamma + 3V \ddot{\gamma} \cos \gamma \\ \quad - 3V \dot{\gamma} \ddot{\gamma} \sin \gamma - V \dot{\gamma}^3 \cos \gamma + V \ddot{\gamma} \cos \gamma, \end{cases} \quad (30)$$

where $\omega_1 = \partial f_1(\mathbf{x}) / \partial \mathbf{x}$, $\omega_2 = \partial f_2(\mathbf{x}) / \partial \mathbf{x}$, $\Omega_1 = \partial \omega_1(\mathbf{x}) / \partial \mathbf{x}$, and $\Omega_2 = \partial \omega_2(\mathbf{x}) / \partial \mathbf{x}$. According to Eqs. (28) and (30), the output dynamics can be written as

$$\begin{bmatrix} \ddot{V} \\ h^{(4)} \end{bmatrix} = \mathbf{F}^*(\mathbf{x}) + \mathbf{G}^*(\mathbf{x})\mathbf{u}. \quad (31)$$

The detailed expressions of ω_1 , ω_2 , Ω_1 , Ω_2 , \mathbf{F}^* , and \mathbf{G}^* are given in Appendix. The determinant of $\mathbf{G}^*(\mathbf{x})$ is

$$\det[\mathbf{G}^*(\mathbf{x})] = \left(T + \frac{\partial L}{\partial \alpha} \cos \alpha + \frac{\partial D}{\partial \alpha} \sin \alpha \right) \cos \gamma, \quad (32)$$

and $\mathbf{G}^*(\mathbf{x})$ can be nonsingular under the condition

$$\det[\mathbf{G}^*(\mathbf{x})] \neq 0 \Leftrightarrow \left(T + \frac{\partial L}{\partial \alpha} \cos \alpha + \frac{\partial D}{\partial \alpha} \sin \alpha \right) \cos \gamma \neq 0. \quad (33)$$

Therefore, $\mathbf{G}^*(\mathbf{x})$ is nonsingular unless flight path angle γ is vertical or

$$T + \frac{\partial L}{\partial \alpha} \cos \alpha + \frac{\partial D}{\partial \alpha} \sin \alpha = 0.$$

Eq. (31) can be rewritten in a decoupled-integrator form as

$$\begin{cases} \mathbf{u} = [\mathbf{G}^*(\mathbf{x})]^{-1} [\mathbf{v} - \mathbf{F}^*(\mathbf{x})], \\ \mathbf{v} = [v_1, v_2]^T = [\ddot{v}, h^{(4)}]^T. \end{cases} \quad (34)$$

3.2 LQR design

The objective of control system design is to track the desired command and eliminate input/output errors. Using Eqs. (28) and (30), we define a nonlinear coordinate transformation $\xi = T_1[\mathbf{x}, V_d(t)]$ and $\eta = T_2[\mathbf{x}, h_d(t)]$ as

$$\xi_1 = V - V_d, \quad \xi_2 = \dot{V} - \dot{V}_d, \quad \xi_3 = \ddot{V} - \ddot{V}_d, \quad (35)$$

$$\eta_1 = h - h_d, \quad \eta_2 = \dot{h} - \dot{h}_d, \quad \eta_3 = \ddot{h} - \ddot{h}_d. \quad (36)$$

Then two subsystems are obtained as follows:

$$\dot{\xi} = \mathbf{A}_1 \xi + \mathbf{b}_1 v_1, \quad (37)$$

$$\dot{\eta} = \mathbf{A}_2 \eta + \mathbf{b}_2 v_2, \quad (38)$$

where

$$\mathbf{A}_1 = \begin{bmatrix} 0 & 1 & 0 \\ 0 & 0 & 1 \\ 0 & 0 & 0 \end{bmatrix}, \quad \mathbf{b}_1 = \begin{bmatrix} 0 \\ 0 \\ 1 \end{bmatrix}, \quad (39)$$

$$A_2 = \begin{bmatrix} 0 & 1 & 0 & 0 \\ 0 & 0 & 1 & 0 \\ 0 & 0 & 0 & 1 \\ 0 & 0 & 0 & 0 \end{bmatrix}, \quad b_2 = \begin{bmatrix} 0 \\ 0 \\ 0 \\ 1 \end{bmatrix}. \quad (40)$$

We design two LQRs for the two linear subsystems (37) and (38). Consider the intermediate objective functions

$$J_1 = \int_0^\infty (\xi^T Q_1 \xi + r_1 v_1^2) dt, \quad (41)$$

and

$$J_2 = \int_0^\infty (\eta^T Q_2 \eta + r_2 v_2^2) dt. \quad (42)$$

Then, the two auxiliary control inputs are derived by minimizing J_1 and J_2 subject to subsystems (37) and (38), respectively:

$$v = \begin{bmatrix} v_1 \\ v_2 \end{bmatrix} = \begin{bmatrix} -r_1^{-1} b_1^T P_1 \xi \\ -r_2^{-1} b_2^T P_2 \eta \end{bmatrix}, \quad (43)$$

where P_1 and P_2 are the positive-definite solutions to the Riccati equations:

$$A_1^T P_1 + P_1 A_1 - r_1^{-1} P_1 b_1 b_1^T P_1 + Q_1 = 0 \quad (r_1, Q_1 > 0), \quad (44)$$

$$A_2^T P_2 + P_2 A_2 - r_2^{-1} P_2 b_2 b_2^T P_2 + Q_2 = 0 \quad (r_2, Q_2 > 0), \quad (45)$$

where $r_1, r_2, Q_1 = \text{diag}\{q_{11}, q_{12}, q_{13}\}$, and $Q_2 = \text{diag}\{q_{21}, q_{22}, q_{23}, q_{24}\}$ are the controller design parameters. The nonlinear control law u is acquired by combining Eqs. (34) and (43):

$$u = [G^*(x)]^{-1} \begin{bmatrix} -r_1^{-1} b_1^T P_1 \xi \\ -r_2^{-1} b_2^T P_2 \eta \end{bmatrix} - F^*(x). \quad (46)$$

4 Tracking controller design

The nonlinear control law defined by Eq. (46) is designed based on the precise system model (where the system uncertainty is $\Delta=0$). However, if the system uncertainties are not ignored, the dynamical inverse of the plant will deviate from the nominal value, which prevents the system from meeting the design requirements. Therefore, while designing the control law, we employ SRA to analyze the system stability and performance. Subsequently, an optimization algorithm is applied to find the optimal parameters of the controller, which maximizes the system robustness. The flow diagram of LQR design based on SRA is shown in Fig. 1.

4.1 Design parameter selection

In Eq. (46), the design parameter vector is defined as

$$p = [r_1, q_{11}, q_{12}, q_{13}, r_2, q_{21}, q_{22}, q_{23}, q_{24}]^T. \quad (47)$$

In the closed-loop control system, there is a certain map between the design requirements and design parameters. Thus, the design parameter space is constructed according to the allowable variation range of design requirements.

4.2 Stochastic robustness measurement

In this section we introduce the measurements of stochastic robustness. A detailed theoretical description can be seen in Stengel and Ryan (1991) and Wang and Stengel (2001; 2002). The concept of stochastic robustness includes stochastic stability and stochastic performance analyses. For each design stability and performance requirement, define a corresponding binary indicator function $I[\cdot]$ as 1 if an acceptable system appears and as 0 otherwise. The probability of design requirement P_r can be calculated by an integral

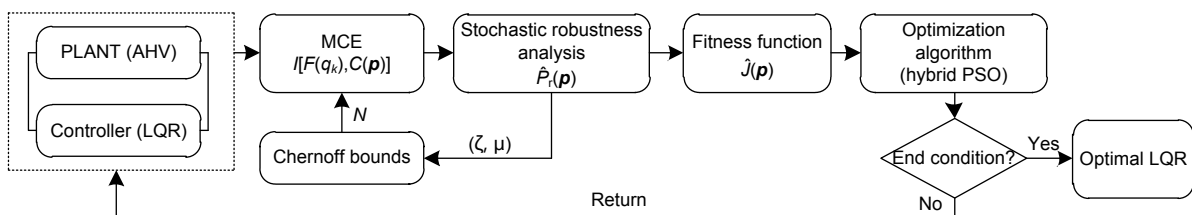


Fig. 1 Flow diagram of linear-quadratic regulator design based on stochastic robustness analysis

of the corresponding indicator function over the expected system parameter space. The stochastic robustness analysis is based on the fitness function formalized by combining the probabilities of various design requirements with certain weights.

It is well-known that MCE has been widely used to estimate probabilities. The estimates of the probability and fitness function based on N samples are as follows (Wang and Stengel, 2002):

$$\hat{P}_r(\mathbf{p}) = \frac{1}{N} \sum_{k=1}^N I[F(q_k), C(\mathbf{p})], \quad (48)$$

$$\hat{J}(\mathbf{p}) = f(P_{r1}(\mathbf{p}), P_{r2}(\mathbf{p}), \dots), \quad (49)$$

where $F(q_k)$ is the plant structure with system parameter q_k selected randomly throughout the parameter space and $C(\mathbf{p})$ is the designed controller with design parameter \mathbf{p} . The estimated fitness function, \hat{J} , approaches the true fitness J in the limit as $N \rightarrow \infty$.

There are three aspects of flight control robustness for hypersonic flight vehicles, stability, performance in velocity tracking response, and performance in altitude tracking response, which are considered as the evaluative indices for robustness analysis. Table 2 lists the fitness function chosen to guide the optimal search algorithm, which is a weighted sum of 22 probabilities of design requirements:

$$J(\mathbf{p}) = \sum_{j=1}^{22} \omega_j P_j(\mathbf{p}), \quad (50)$$

where ω_j are the weights for the probabilities of various design requirements.

4.3 Application of the Chernoff bound

SRA is based on a stochastic evaluation, such as MCE. The important process is to specify the estimated probability of the stochastic algorithm within a prior specified accuracy $\zeta \in (0, 1)$ from the true value and with a special confidence $1 - \mu$, $\mu \in (0, 1)$. This means that the algorithm can successfully return an approximately correct estimate with a probability of $1 - \mu$. The key problem is how to determine the sample size N to guarantee the suitable estimated accuracy and confidence.

Definition 1 (Piccoli et al., 2009) For a stochastic process, let $\zeta \in (0, 1)$ and $\mu \in (0, 1)$ be the assigned

Table 2 Stability and performance metrics for a hypersonic flight vehicle

Metric number	Weight in $J(\mathbf{p})$	Design requirement
1 (2)	10.0 (10.0)	System stability in velocity response (altitude response)
3 (4)	2.0 (2.0)	No reversal in velocity response (altitude response) before peaking
5 (6)	2.0 (0.5)	Steady error in velocity response less than 2.5% (5.0%)
7 (8)	2.0 (0.5)	Steady error in altitude response less than 5.0% (10%)
9 (10)	2.0 (0.5)	Overshoot in velocity response less than 10% (20%)
11 (12)	2.0 (0.5)	Overshoot in altitude response less than 20% (40%)
13 (14)	2.0 (0.5)	90% rise time in velocity response less than 25 s (50 s)
15 (16)	2.0 (0.5)	90% rise time in altitude response less than 50 s (100 s)
17 (18)	2.0 (0.5)	10% settling time in velocity response less than 25 s (50 s)
19 (20)	2.0 (0.5)	10% settling time in altitude response less than 50 s (100 s)
21 (22)	5.0 (0.5)	Maximum change in angle of attack less than 3° (5°)

probability levels. The stochastic algorithm is successful if it returns, with a probability of at least $1 - \mu$, an estimate $\hat{P}_r(\mathbf{p})$ of the true probability of performance $P_r(\mathbf{p})$ with an error of at most size ζ . Equivalently stated,

$$P\left(\left|\hat{P}_r(\mathbf{p}) - P_r(\mathbf{p})\right| > \zeta\right) \leq \mu. \quad (51)$$

Bounds on the needed samples can be achieved using the well-known Chernoff bounds, which are demonstrated by the following definition:

Definition 2 (Chernoff bound) (Chernoff, 1952) For any $\zeta \in (0, 1)$ and $\mu \in (0, 1)$, if the sample size

$$N \geq \frac{1}{2\zeta^2} \ln \frac{2}{\mu}, \quad (52)$$

then the estimated probability is greater than $1 - \mu$, and

$$\left|\hat{P}_r(\mathbf{p}) - P_r(\mathbf{p})\right| \leq \zeta.$$

In other words, Eq. (51) holds true. We can make good use of Chernoff bounds, as shown in

Algorithm 1, to provide information on robustness in estimating the probabilities.

Algorithm 1 Chernoff bounds applied for stochastic evaluation

Input: probability levels $\zeta, \mu \in (0, 1)$ and the desired performance requirements

Output: empirical probability $\hat{P}_i(\mathbf{p})$ for the specified design requirements

1. Determine the finite sample size $N=f(\zeta, \mu)$ by setting the expression in Eq. (52)
 2. Draw N samples for the MCE test as (q_1, q_2, \dots, q_N)
 3. Return $\hat{P}_i(\mathbf{p})$
-

4.4 Optimal design of system robustness

The target of robust LQR design is to choose the design parameters \mathbf{p} to guarantee system robustness, which fulfills the design requirements on the stability and performance of the system without influencing the system uncertainties. The key problem of robust LQR design is to find the optimal design parameters \mathbf{p}^* in the design parameter space to maximize the probability of desired system stability and performance. However, contradictions between system stability and performance always exist in a closed-loop control system. Therefore, to achieve the optimal tradeoff between system stability and system performance, optimization techniques are commonly used.

Subject to the fitness function described by Eq. (50), two cases are considered:

Case 1: $P_{rj}(\mathbf{p})$ is maximized.

Case 2: Under the requirement of system reliability, $P_{rj}(\mathbf{p})$ is large enough.

If any one of the two cases occurs, it can be said that the robust LQR design is successful. Furthermore, if the optimal design parameters \mathbf{p}^* cannot fulfill the design requirements, LQR can be redesigned by modifying the design requirements or changing the design parameter space.

5 Improved hybrid PSO algorithm

To search for the optimal design parameters, in this section we propose a specific improved hybrid

PSO algorithm. Compared with conventional optimization algorithms, the proposed algorithm presents a higher search ability.

5.1 Algorithm introduction

The genetic algorithm (GA) is a class of random search methods that imitate natural evolution. Through simple coding techniques and evolution manipulations, GA completes searches by mimicking natural competitions. Although GA is a probability algorithm, it is quite different from general stochastic algorithms, which organically combine directional search with random search (Goldberg, 1989). Additionally, GA has potential parallelism, which can compare different individuals simultaneously. As a result of failing to return population information, the algorithm requires more training time to obtain the exact solution. In addition, if the initial population, crossover probability, and mutation probability selections are unsuitable, early convergence will typically occur.

The PSO algorithm was proposed as a bionic algorithm, which searches for the optimal solution in a multidimensional space through cooperation among individuals (Kennedy and Eberhart, 1995). The basic idea of PSO is to simulate bird predation. Each particle moves in the solution space and records the best points (both particle and population points). Particles update their own velocity and position based on the two best points. By constantly updating the extreme points, the PSO algorithm quickly determines the optimal configuration.

Considering GA's high local convergence rate, when the iteration achieves the local area around the global optimal solution, we choose GA to compensate for the slow search speed of PSO algorithms in the local space. Fig. 2 shows the sketch of this new hybrid PSO algorithm. Starting from the initial point \mathbf{x}_0 , the PSO algorithm is used to quickly search the whole solution space R_n . When the population of the PSO algorithm is achieved around the local area U of the global optimal solution, GA replaces PSO to continue

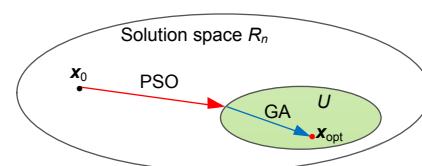


Fig. 2 Sketch of the new hybrid PSO algorithm

the search. After an appropriate number of iterations, the optimal global solution x_{opt} is obtained.

Whether the proposed hybrid PSO algorithm can run effectively relies on the global search ability of PSO and the local convergence velocity of GA. To enhance the ability of global search, PSO is improved by adopting four techniques: uniform initialization of population, adaptive Sigmoid inertia weight (Malik *et al.*, 2007), asynchronous change in learning factors (Ratnaweera *et al.*, 2004), and time factor adjusting to weights. To promote the local convergence rate of GA, the mutation operator is canceled artificially, and the iteration will be implemented in an enclosed space and achieve a fast convergence.

5.2 Algorithm procedure

The procedure of the novel hybrid multi-objective PSO algorithm is shown in Fig. 3. The algorithm procedures can be described as follows:

1. Given an optimization problem, a mathematical method is used to describe the actual problem in the standard form of a general optimization problem.
2. The PSO algorithm is applied to deal with the optimization problem preliminarily.
3. When the iteration of the PSO algorithm achieves the local area of the global optimal solution, combining with the global suboptimal solution, a new population is generated.
4. Beginning with the new population, GA is used to quickly search the neighborhood of the global optimal solution, and the global optimal solution is finally obtained.

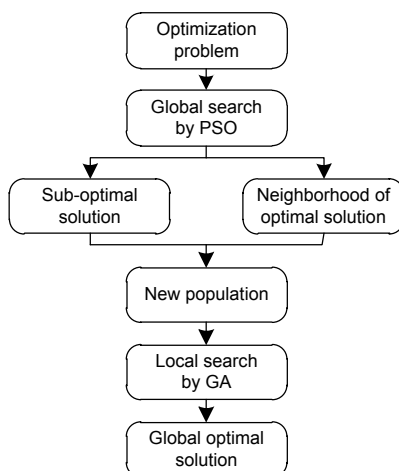


Fig. 3 Algorithm procedure

5.3 Algorithm testing cases

In this section, we employ three nonlinear benchmark functions to verify the effectiveness of the proposed hybrid PSO algorithm. The first function is the Alpine function:

$$f_1 = -\sin x_1 \sin x_2 \sqrt{x_1 x_2}, \quad (53)$$

where $x_1, x_2 \in [0, 10]$. The Alpine function has a lot of local extreme points, but only a global minimum $f_1^* = -7.8856$ ($x_1 = x_2 = 7.917$). The second function is the Rastrigrin function:

$$f_2 = \sum_{i=1}^2 [x_i^2 - 10 \cos(2\pi x_i) + 10], \quad (54)$$

where $x_1, x_2 \in (-10, 10)$. The Rastrigrin function is a multi-peak function, and obtains the global minimum $f_2^* = 0$ when $x_1 = x_2 = 0$. The third function is the Schaffer function:

$$f_3 = 0.5 + \frac{\sin^2 \sqrt{x_1^2 + x_2^2} - 0.5}{[1 + 0.001(x_1^2 + x_2^2)]^2}, \quad (55)$$

where $x_1, x_2 \in [-10, 10]$. The Schaffer function has only a global minimum $f_3^* = 0$ when $x_1 = x_2 = 0$.

We use generic GA, generic PSO, and the improved hybrid PSO algorithm proposed in this study (denoted as improved PSO) to search for the minimum points of the aforementioned testing functions. Each testing experiment is repeated 2000 times. The parameter setting of algorithms and the testing results are illustrated in Table 3. Compared to generic GA and generic PSO, the improved PSO presents the mean results closest to the global minimum and the smallest standard deviations. Furthermore, the probabilities of reaching the optimal value (denoted as the success rate) of the improved PSO algorithm are 89.4%, 90.2%, and 75.2%, respectively, for the three functions, which are the highest values among the three algorithms. These testing results indicate that the improved hybrid PSO algorithm has better search ability and robustness.

Table 3 Parameter settings and testing results with a population size of 26

Function	Algorithm	Maximum number of iterations	Mean optimal value	Standard deviation	Success rate (%)
Alpine	Generic GA	30	-7.5360	0.9869	37.35
	Generic PSO	30	-7.4844	1.0462	87.20
	Improved PSO	25 for PSO; 5 for GA	-7.5545	0.9612	89.40
Rastrigrin	Generic GA	100	0.1434	0.3687	83.35
	Generic PSO	100	0.0530	0.0633	3.00
	Improved PSO	90 for PSO; 10 for GA	0.0434	0.1948	90.20
Schaffer	Generic GA	180	0.0091	0.0034	8.20
	Generic PSO	180	0.0036	0.0043	67.00
	Improved PSO	170 for PSO; 10 for GA	0.0025	0.0041	75.20

6 Simulation results

6.1 Optimal algorithm analysis

Given the same initial value, three optimal algorithms, the improved hybrid PSO, generic GA, and generic PSO, are used to search for the control parameters of the AHV controller. The parameter allocations for optimal algorithms are shown in Table 4.

Table 4 Allocation of algorithm parameters

Algorithm	Particle/chromosome number	Maximum number of iterations
Generic GA	50	20
Generic PSO	16	20
Improved PSO	16	15 for PSO; 5 for GA

The simulation results are shown in Fig. 4. The x axis represents the number of iterations and the y axis represents the maximum value of fitness functions of all the population. The fitness function defined in this study presents the fitness of particle or chromosome in the population, and the objective is to determine the parameters with the maximum fitness value. Fig. 4 shows that the generic GA achieves earlier convergence due to the insufficient population size, which causes insufficient population diversity. The generic PSO algorithm drops into the local area after 15 iterations and the maximum value of the fitness function stops at 45.20. The improved PSO algorithm increases the maximum value of the fitness function to 46.38. Through simulation and comparative analysis, we can say that the improved PSO algorithm presents a better performance than the generic GA and generic PSO algorithms for control parameter determination.

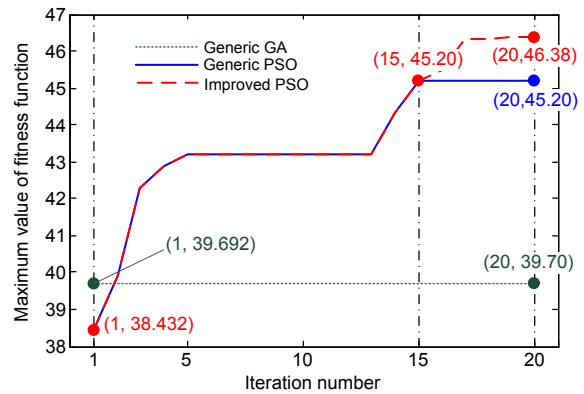


Fig. 4 Comparison of optimization algorithms

6.2 Robustness analysis

Chernoff bounds are used to determine the finite sample size N for MCE simulation. Set $\mu=0.025$, which means the confidence is 97.5%. By setting estimate error $\zeta=0.1$, the sample size N for stochastic evaluation can be calculated by

$$N = \frac{1}{2\zeta^2} \ln \frac{2}{\mu} \approx 219.1.$$

The larger the number of samples, the higher the estimation accuracy. In this study, we choose $N=230$ and it can be inferred that the accuracy is high. The simulation results in Fig. 4 also indicate that the accuracy when $N=230$ is high enough to present the characteristics of the closed-loop system. Then, the probability of each requirement can be estimated:

$$P\left(\left|P_r(\mathbf{p}) - \hat{P}_r(\mathbf{p})\right| \leq 0.1\right) > 97.5\%.$$

This emphasizes that the estimated probability of the desired design from the MCE test with an error from the true values of less than 10% has a confidence of larger than 97.5%.

6.3 Results of control design

The control system structure designed in this study is shown in Fig. 5. The design parameter space is given in Table 5.

Table 5 Design parameter space

Parameter	Bound
r_1	(0.01, 10)
q_{11}	(0.01, 10)
q_{12}	(0.1, 100)
q_{13}	(0.1, 200)
r_2	(0.01, 10)
q_{21}	(0.01, 10)
q_{22}	(0.1, 200)
q_{23}	(0.1, 300)
q_{24}	(0.1, 400)

The ranges of the additive parametric uncertainties used in the simulations are taken as follows:

$$|\Delta m| \leq 3\%, |\Delta I| \leq 2\%, |\Delta S| \leq 2\%, |\Delta \bar{c}| \leq 2\%,$$

$$|\Delta \rho| \leq 6\%, |\Delta c_e| \leq 3\%, |\Delta C_{M_1}^\alpha| \leq 10\%. \quad (56)$$

After 15 global search iterations by the PSO algorithm and five generations of quick evolution by GA, the optimal parameter vector (Eq. (47)) is found to be

$$p^* = [1.8374, 4.2973, 77.5720, 130.2691, 5.8562, 0.4486, 53.8780, 259.4353, 275.6245].$$

Substituting p^* into the Riccati equations (Eqs. (44) and (45)), the positive-definite matrices P_1 and P_2 are calculated as

$$P_1 = \begin{bmatrix} 23.655 & 26.32 & 2.81 \\ 26.32 & 142.072 & 15.4678 \\ 2.81 & 15.4678 & 17.2104 \end{bmatrix},$$

$$P_2 = \begin{bmatrix} 6.2641 & 16.7964 & 13.3452 & 1.6208 \\ 16.7964 & 221.1962 & 184.7278 & 22.6329 \\ 13.3452 & 184.7278 & 477.0357 & 60.6870 \\ 1.6208 & 22.6329 & 60.6870 & 48.2172 \end{bmatrix}.$$

To illustrate the advantages and effectiveness of the controllers proposed in this study (denoted as LQR-SRA), the sliding mode controller (SMC) is designed in both velocity and altitude channels. Details of SMC were presented in Fernández and Hedrick (1987). The sliding surfaces are designed as

$$\sigma_v = \left(\frac{d}{dt} + \lambda_1 \right)^2 e_v, \quad \sigma_h = \left(\frac{d}{dt} + \lambda_2 \right)^2 e_h,$$

where λ_1 and λ_2 are design parameters and $e_v = \zeta_1$ and $e_h = \eta_1$ are the velocity tracking error and altitude tracking error, respectively. Let $\dot{\sigma}_v = -k_1 \text{sign}(\sigma_v)$ and $\dot{\sigma}_h = -k_2 \text{sign}(\sigma_h)$. Combined with Eq. (34), the control law of SMC is obtained as

$$u = [G^*(x)]^{-1} \cdot \left[\begin{array}{c} -2\lambda_1 \ddot{e}_v - \lambda_1^2 \dot{e}_v - k_1 \text{sign}(\sigma_v) \\ -3\lambda_2 \ddot{e}_h - 3\lambda_2^2 \dot{e}_h - \lambda_2^3 e_h - k_2 \text{sign}(\sigma_h) \end{array} \right] - F^*(x), \quad (57)$$

where $\text{sign}(\cdot)$ is the sign function and k_1 and k_2 are the positive design parameters. In this simulation, the design parameters of SMC are set as $\lambda_1=0.2$, $\lambda_2=0.2$, $k_1=5$, and $k_2=10$.

The performances of the tracking velocity command and altitude command with nominal parameters are shown in Figs. 6 and 7, respectively.

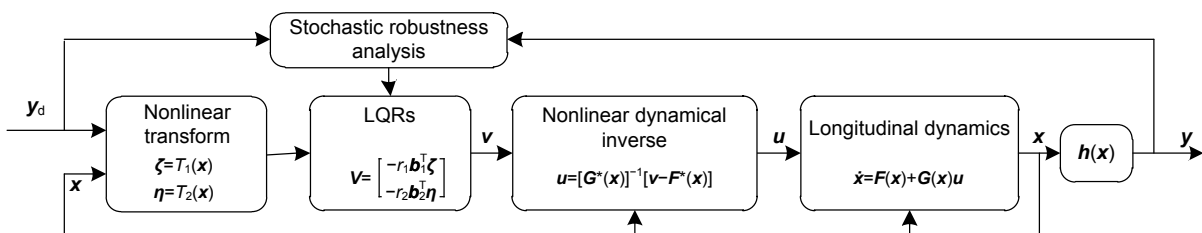


Fig. 5 Control system structure

Fig. 6 shows a comparison of the system response due to a 100-ft/s step-velocity change command from the trimmed condition between SMC and the proposed controller (LQR-SRA). For LQR-SRA, the velocity converges to 90% of the command value within 11 s with a maximum change in altitude of less than 20 ft (1% of the command value) and a maximum change in angle of attack of less than 1.5° . Fig. 7 shows a comparison of the system response due to a 2000-ft step-altitude change command from the trimmed condition between SMC and LQR-SRA. For LQR-SRA, the altitude converges to 90% of the command value within 28 s with a maximum change in velocity of less than 6 ft/s and a maximum change in angle of attack of less than 3.0° .

As shown in Figs. 6 and 7, compared to SMC, LQR-SRA shows faster convergence and more steady tracking trajectories in both velocity and altitude channels, and offers more steady elevator deflection. In contrast, the control inputs of SMC present high-frequency chattering in elevator deflection. Therefore, the closed-loop system controlled by LQR-SRA has a better performance for the tracking velocity command and altitude command.

Assume that all of the parametric uncertainties are subject to uniform distribution, and the bounds are subject to Eq. (56). The stochastic responses of the closed-loop control system to the 100-ft/s step-velocity command and 2000-ft step-altitude

command are illustrated in Figs. 8 and 9, respectively. As shown, the closed-loop system presents good tracking performances in the velocity channel and altitude channel, in spite of the vibration of nominal parameters. For all of the tracking trajectories, there is almost no static tracking error in the velocity channel, and the maximum static tracking error in the altitude channel is less than 2% with respect to the nominal value of 2000 ft, which meets the requirements of engineering applications. Both figures confirm that the LQRs designed in this study achieve good robustness in the presence of parametric uncertainties.

7 Conclusions

This paper provides a robust LQR design strategy for AHVs based on SRA. The general LQR theory was applied for a nonlinear system control. We deduced the nonlinear dynamic inverse of the longitudinal dynamics with seven elements of the system state variable. Chernoff bounds were used to determine a finite sample size $N=230$ for the Monte Carlo evaluation test with the desired probability levels as $\zeta=0.1$ and $\mu=0.025$, which guarantees the robustness of stochastic evaluation. To search for the best design parameters of LQRs, we proposed an improved hybrid multi-objective PSO algorithm. Simulation results demonstrated that the improved hybrid PSO

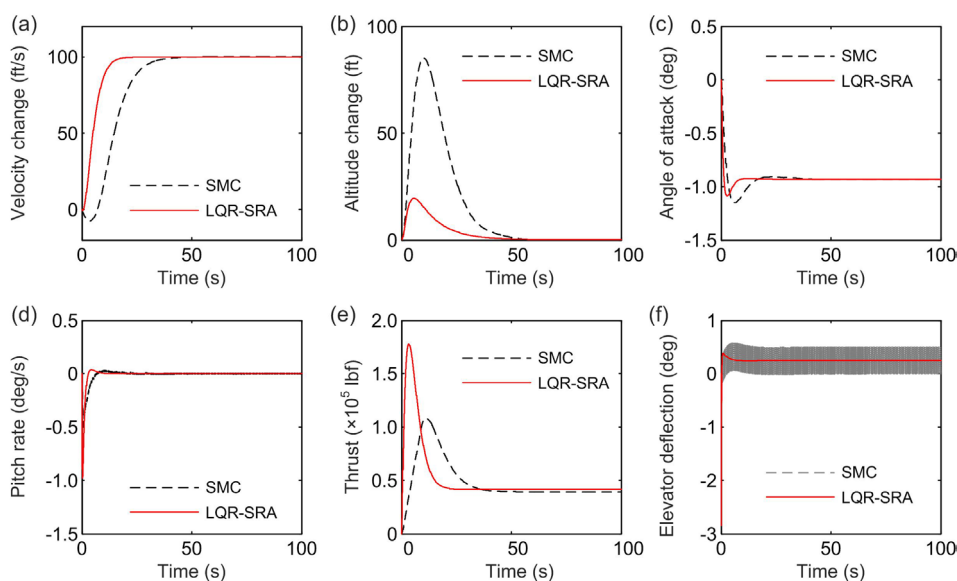


Fig. 6 Comparisons of SMC and LQR-SRA responses to a 100-ft/s step-velocity command with nominal parameters: (a) velocity change; (b) altitude change; (c) angle of attack; (d) pitch rate; (e) thrust; (f) elevator deflection

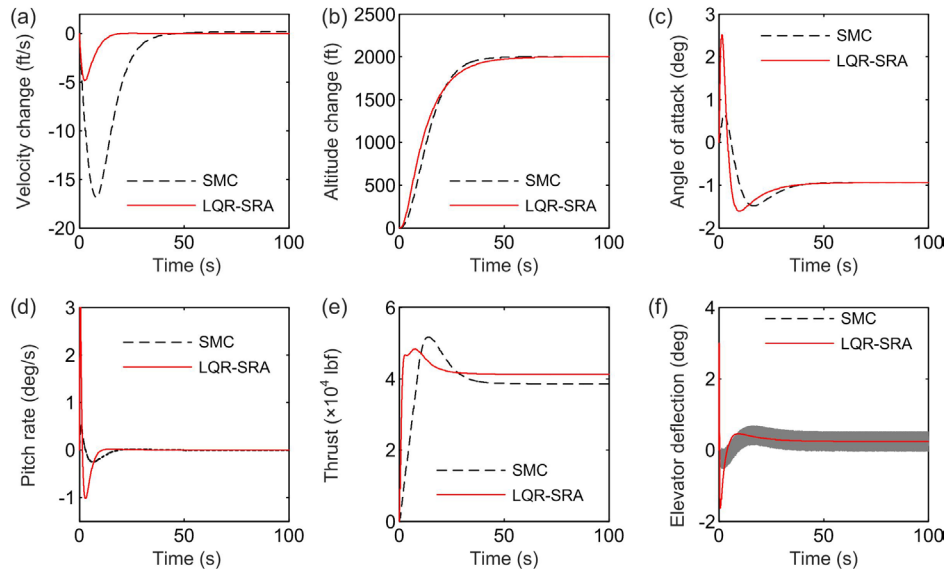


Fig. 7 Comparisons of SMC and LQR-SRA responses to a 2000-ft step-altitude command with nominal parameters: (a) velocity change; (b) altitude change; (c) angle of attack; (d) pitch rate; (e) thrust; (f) elevator deflection

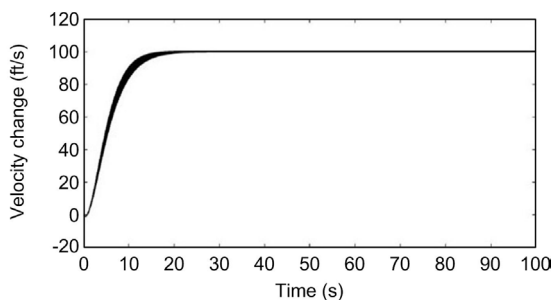


Fig. 8 Stochastic response with LQR-SRA to a 100-ft/s step-velocity command

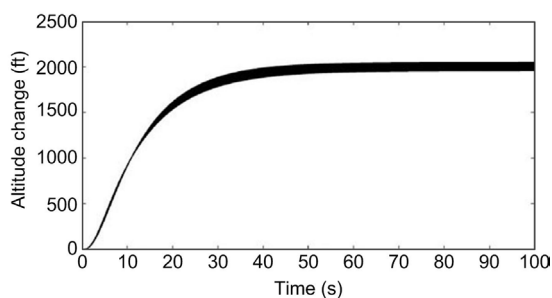


Fig. 9 Stochastic response with LQR-SRA to a 2000-ft step-altitude command

algorithm can effectively determine the best solution to LQR parameters in a large design parameter space. According to the response to a 100-ft/s step-velocity command and a 2000-ft step-altitude command, the optimal LQRs have good performance and robustness in the presence of parametric uncertainties.

Our future work will focus on higher-order sliding mode control and fractional-order control for flight control of hypersonic flight vehicles, and comparisons will be made with the controllers proposed in this paper.

References

- Arun Kishore, W.C., Sen, S., Ray, G., *et al.*, 2008. Dynamic control allocation for tracking time-varying control demand. *J. Guid. Contr. Dynam.*, **31**(4):1150-1157. <https://doi.org/10.2514/1.34085>
- Bolender, M.A., Doman, D.B., 2005. A non-linear model for the longitudinal dynamics of a hypersonic air-breathing vehicle. AIAA Guidance, Navigation, and Control Conf. and Exhibit, p.2005-6255. <https://doi.org/10.2514/6.2005-6255>
- Bolender, M., Oppenheimer, M., Doman, D., 2007. Effects of uncertainty and viscous aerodynamics on dynamics of a flexible air-breathing hypersonic vehicle. AIAA Atmospheric Flight Mechanics Conf. and Exhibit, p.2007-6397. <https://doi.org/10.2514/6.2007-6397>
- Chernoff, H., 1952. A measure of asymptotic efficiency for tests of a hypothesis based on the sum of observations. *Ann. Math. Stat.*, **23**:493-507. <https://doi.org/10.1214/aoms/1177729330>
- Dickeson, J.J., Rodriguez, A.A., Sirdharan, S., *et al.*, 2009. Decentralized control of an air-breathing scramjet-powered hypersonic vehicle. AIAA Guidance, Navigation and Control Conf., p.2009-6281. <https://doi.org/10.2514/6.2009-6281>
- Fernández, B.R., Hedrick, J.K., 1987. Control of multivariable nonlinear systems by the sliding mode method. *Int. J.*

- Contr.*, **46**(3):1019-1040.
<https://doi.org/10.1080/00207178708547410>
- Fidan, B., Mirmirani, M., Ioannou, P.A., 2003. Flight dynamics and control of air-breathing hypersonic vehicles: reviews and new directions. *AIAA Int. Space Planes and Hypersonic Systems and Technologies*, p.2003-7081.
<https://doi.org/10.2514/6.2003-7081>
- Ge, D.M., Huang, X.L., Gao, H.J., 2011. Multi-loop gain-scheduling control of flexible air-breathing hypersonic vehicle. *Int. J. Innov. Comput. Inform. Contr.*, **7**(10): 5865-5880.
- Goldberg, D.E., 1989. *Genetic Algorithms in Search, Optimization and Machine Learning*. Addison-Wesley Publishing Company Inc., Reading.
- Grove, K.P., Sigthorsson, D.O., Serrani, A., et al., 2005. Reference command tracking for a linearized model of an air-breathing hypersonic vehicle. *AIAA Guidance, Navigation, and Control Conf. and Exhibit*, p.2005-6144.
<https://doi.org/10.2514/6.2005-6144>
- Kennedy, J., Eberhart, R.C., 1995. Particle swarm optimization. *Proc. IEEE Int. Conf. on Neural Networks*, p.1942-1948.
<https://doi.org/10.1109/ICNN.1995.488968>
- Kuipers, M.K., Ioannou, P., Fidan, B., et al., 2008. Robust adaptive multiple model controller design for an air-breathing hypersonic vehicle model. *AIAA Guidance, Navigation and Control Conf. and Exhibit*, p.2008-7142.
<https://doi.org/10.2514/6.2008-7142>
- Malik, R.F., Rahman, T.A., Hashim, S.Z.M., et al., 2007. New particle swarm optimizer with Sigmoid increasing inertia weight. *Int. J. Comput. Sci. Secur.*, **1**(2):35-44.
- Marrison, C.I., Stengel, R.F., 1997. Robust control system design using random search and genetic algorithms. *IEEE Trans. Autom. Contr.*, **42**(6):835-839.
<https://doi.org/10.1109/9.587338>
- Marrison, C.I., Stengel, R.F., 1998. Design of robust control systems for a hypersonic aircraft. *J. Guid. Contr. Dynam.*, **21**(1):58-63. <https://doi.org/10.2514/2.4197>
- Parker, J.T., Serrani, A.S., Yurkovich, M.A., et al., 2007. Control-oriented modeling of an air-breathing hypersonic vehicle. *J. Guid. Contr. Dynam.*, **30**(3):856-869.
<https://doi.org/10.2514/1.27830>
- Piccoli, B., Zadarnowska, K., Gaeta, M., 2009. Stochastic algorithms for robustness of control performances. *Automatica*, **45**(6):1407-1414.
<https://doi.org/10.1016/j.automatica.2009.02.018>
- Preller, D., Smart, M.K., 2015. Longitudinal control strategy for hypersonic accelerating vehicles. *J. Spacecr. Rock.*, **52**(3):993-999. <https://doi.org/10.2514/1.A32934>
- Pu, Z.P., Tan, X.M., Fan, G.L., et al., 2014. Uncertainty analysis and robust trajectory linearization control of a flexible air-breathing hypersonic vehicle. *Acta Astronaut.*, **101**:16-32.
<https://doi.org/10.1016/j.actaastro.2014.01.025>
- Ratnaweera, A., Halgamuge, S.K., Watson, H.C., 2004. Self-organizing hierarchical particle swarm optimizer with time-varying acceleration coefficients. *IEEE Trans. Evol. Comput.*, **8**(3):240-255.
<https://doi.org/10.1109/TEVC.2004.826071>
- Ray, L.R., Stengel, R.F., 1990. Stochastic performance robustness of aircraft control system. *AIAA Paper*, p.1990-3410. <https://doi.org/10.2514/6.1990-3410>
- Rehman, O.U., Petersen, I.R., Fidan, B., 2013. Feedback linearization-based robust nonlinear control design for hypersonic flight vehicles. *J. Syst. Contr. Eng.*, **227**(1): 3-11. <https://doi.org/10.1177/0959651812447722>
- Rodriguez, A.A., Dickeson, J.J., Cifdaloz, O., et al., 2008. Modeling and control of scramjet-powered hypersonic vehicles: challenges, trends, & tradeoffs. *AIAA Guidance, Navigation and Control Conf. and Exhibit*, p.2008-6793.
<https://doi.org/10.2514/6.2008-6793>
- Stengel, R.F., Ryan, L.E., 1989. Multivariable histograms for analysis of linear control system robustness. *American Control Conf.*, p.937-945.
<https://doi.org/10.1109/ACC.1989.4173342>
- Stengel, R.F., Ryan, L.E., 1991. Stochastic robustness of linear time-invariant control systems. *IEEE Trans. Autom. Contr.*, **36**(1):82-87. <https://doi.org/10.1109/9.62270>
- Wang, Q., Stengel, R.F., 2000. Robust nonlinear control of a hypersonic aircraft. *J. Guid. Contr. Dynam.*, **23**(4): 577-585. <https://doi.org/10.2514/2.4580>
- Wang, Q., Stengel, R.F., 2001. Searching for robust minimal-order compensators. *J. Dynam. Syst. Meas. Contr.*, **123**(2): 233-236. <http://doi.org/10.1115/1.1367270>
- Wang, Q., Stengel, R.F., 2002. Robust control of nonlinear systems with parametric uncertainty. *Automatica*, **38**(9): 1591-1599.
[https://doi.org/10.1016/S0005-1098\(02\)00046-8](https://doi.org/10.1016/S0005-1098(02)00046-8)
- Williams, T., Bolender, M., Doman, D., et al., 2006. An aerothermal flexible mode analysis of a hypersonic vehicle. *AIAA Paper*, p.2006-6647.
<https://doi.org/10.2514/6.2006-6647>
- Xu, B., Shi, Z.K., 2015. An overview on flight dynamics and control approaches for hypersonic vehicles. *Sci. China Inform. Sci.*, **58**(7):070201.
<https://doi.org/10.1007/s11432-014-5273-7>
- Xu, B., Zhang, Y., 2015. Neural discrete back-stepping control of hypersonic flight vehicle with equivalent prediction model. *Neurocomputing*, **154**:337-346.
<http://doi.org/10.1016/j.neucom.2014.11.059>
- Xu, B., Fan, Y.H., Zhang, S.M., 2015a. Minimal-learning-parameter technique based adaptive neural control of hypersonic flight dynamics without back-stepping. *Neurocomputing*, **164**:201-209.
<https://doi.org/10.1016/j.neucom.2015.02.069>
- Xu, B., Yang, C.G., Pan, Y.P., 2015b. Global neural dynamic surface tracking control of strict-feedback systems with application to hypersonic flight vehicle. *IEEE Trans.*

Neur. Netw. Learn. Syst., **26**(10):2563-2575.

<https://doi.org/10.1109/TNNLS.2015.2456972>

Xu, B., Guo, Y.Y., Yuan, Y., et al., 2016. Fault-tolerant control using command-filtered adaptive back-stepping technique: application to hypersonic longitudinal flight dynamics. *Int. J. Adapt. Contr. Signal Process.*, **30**(4): 553-577. <https://doi.org/10.1002/acs.2596>

Xu, H.J., Mirmirani, M.D., Ioannou, P.A., 2004. Adaptive

sliding mode control design for a hypersonic flight vehicle. *J. Guid. Contr. Dynam.*, **27**(5):829-838.

<https://doi.org/10.2514/1.12596>

Zong, Q., Wang, J., Tian, B.L., et al., 2013. Quasi-continuous higher-order sliding mode controller and observer design for flexible hypersonic vehicle. *Aerosp. Sci. Technol.*, **27**(1):127-137. <https://doi.org/10.1016/j.ast.2012.07.004>

Appendix: Expressions of ω_1 , ω_2 , Ω_1 , and Ω_2

Vectors ω_1 , ω_2 , and F^* and matrices Ω_1 , Ω_2 , and G^* presented in input/output feedback linearization for variables V and h , with state variable $x = [V, \gamma, h, \alpha, q, \phi, \dot{\phi}]^T$, are given as follows:

$$\omega_1^T = \frac{\partial f_1(x)}{\partial x} = \begin{bmatrix} \frac{(\partial T / \partial V) \cos \alpha - \partial D / \partial V}{m} \\ \frac{-\mu \cos \gamma}{r^2} \\ \frac{2\mu \sin \gamma}{r^3} \\ \frac{-T \sin \alpha - \partial D / \partial \alpha}{m} \\ 0 \\ \frac{(\partial T / \partial \phi) \cos \alpha}{m} \\ 0 \end{bmatrix} \quad (A1)$$

$$\omega_2^T = \frac{\partial f_2(x)}{\partial x} = \begin{bmatrix} \frac{(\partial T / \partial V) \sin \alpha + \partial L / \partial V}{mV} - \frac{T \sin \alpha + L}{mV^2} + \frac{\mu \cos \gamma}{V^2 r^2} + \frac{\cos \gamma}{r} \\ \frac{\mu \sin \gamma}{Vr^2} - \frac{V \sin \gamma}{r} \\ \frac{2\mu \cos \gamma}{Vr^3} - \frac{V \cos \gamma}{r^2} \\ \frac{T \cos \alpha + \partial T / \partial \alpha}{mV} \\ 0 \\ \frac{(\partial T / \partial \phi) \sin \alpha}{mV} \\ 0 \end{bmatrix} \quad (A2)$$

$$\Omega_1 = \frac{\partial \omega_1(x)}{\partial x} = [\omega_{11}, \omega_{12}, \omega_{13}, \omega_{14}, \omega_{15}, \omega_{16}, \omega_{17}]^T, \quad (A3)$$

where

$$\omega_{11} = \begin{bmatrix} \frac{(\partial^2 T / \partial V^2) \cos \alpha - \partial^2 D / \partial V^2}{m} \\ 0 \\ 0 \\ \frac{-(\partial T / \partial V) \sin \alpha - \partial^2 D / \partial V \partial \alpha}{m} \\ 0 \\ \frac{(\partial^2 T / \partial V \partial \phi) \cos \alpha}{m} \\ 0 \end{bmatrix}, \omega_{12} = \begin{bmatrix} 0 \\ \frac{\mu \sin \gamma}{r^2} \\ \frac{2\mu \cos \gamma}{r^3} \\ 0 \\ 0 \\ 0 \\ 0 \end{bmatrix}, \omega_{13} = \begin{bmatrix} 0 \\ \frac{2\mu \cos \gamma}{r^3} \\ \frac{-6\mu \sin \gamma}{r^4} \\ 0 \\ 0 \\ 0 \\ 0 \end{bmatrix},$$

$$\omega_{14} = \begin{bmatrix} \frac{-(\partial T / \partial V) \sin \alpha - \partial^2 D / \partial \alpha \partial V}{m} \\ 0 \\ 0 \\ \frac{-T \cos \alpha - \partial^2 D / \partial \alpha^2}{m} \\ 0 \\ \frac{-(\partial T / \partial \phi) \sin \alpha}{m} \\ 0 \end{bmatrix}, \omega_{16} = \begin{bmatrix} \frac{(\partial^2 T / \partial \phi \partial V) \cos \alpha}{m} \\ 0 \\ 0 \\ \frac{-(\partial T / \partial \phi) \sin \alpha}{m} \\ 0 \\ \frac{(\partial^2 T / \partial \phi^2) \cos \alpha}{m} \\ 0 \end{bmatrix}, \text{ and } \omega_{15} = \omega_{17} = 0.$$

$$\Omega_2 = \frac{\partial \omega_2(\mathbf{x})}{\partial \mathbf{x}} = [\omega_{21}, \omega_{22}, \omega_{23}, \omega_{24}, \omega_{25}, \omega_{26}, \omega_{27}], \tag{A4}$$

where

$$\omega_{21} = \begin{bmatrix} \frac{(\partial^2 T / \partial V^2) \sin \alpha + \partial^2 L / \partial V^2}{mV} - 2 \frac{(\partial T / \partial V) \sin \alpha + \partial L / \partial V}{mV^2} + 2 \frac{T \sin \alpha + L}{mV^3} - \frac{2\mu \cos \gamma}{V^3 r^2} \\ \frac{\mu \sin \gamma}{V^2 r^2} - \frac{\sin \gamma}{r} \\ \frac{2\mu \cos \gamma}{V^2 r^3} - \frac{\cos \gamma}{r^2} \\ \frac{(\partial T / \partial V) \cos \alpha + \partial^2 L / \partial V \partial \alpha}{mV} - \frac{T \cos \alpha + \partial L / \partial \alpha}{mV^2} \\ 0 \\ \frac{(\partial^2 T / \partial V \partial \phi) \sin \alpha}{mV} - \frac{(\partial T / \partial \phi) \sin \alpha}{mV^2} \\ 0 \end{bmatrix},$$

$$\omega_{22} = \begin{bmatrix} \frac{\mu \sin \gamma}{V^2 r^2} - \frac{\sin \gamma}{r} \\ \frac{\mu \cos \gamma}{V r^2} - \frac{V \cos \gamma}{r} \\ \frac{2\mu \sin \gamma}{V r^3} + \frac{V \sin \gamma}{r^2} \\ 0 \\ 0 \\ 0 \\ 0 \end{bmatrix}, \quad \omega_{23} = \begin{bmatrix} \frac{2\mu \cos \gamma}{V^2 r^3} - \frac{\cos \gamma}{r^2} \\ -\frac{2\mu \sin \gamma}{V r^3} + \frac{V \sin \gamma}{r^2} \\ \frac{6\mu \cos \gamma}{V r^4} + \frac{2V \cos \gamma}{r^3} \\ 0 \\ 0 \\ 0 \\ 0 \end{bmatrix},$$

$$\omega_{24} = \begin{bmatrix} \frac{(\partial T / \partial V) \cos \alpha + \partial^2 L / \partial \alpha \partial V}{mV} - \frac{T \cos \alpha + \partial L / \partial \alpha}{mV^2} \\ 0 \\ 0 \\ \frac{-T \sin \alpha + \partial^2 L / \partial \alpha^2}{mV} \\ 0 \\ \frac{(\partial T / \partial \phi) \cos \alpha}{mV} \\ 0 \end{bmatrix}, \quad \omega_{26} = \begin{bmatrix} \frac{(\partial^2 T / \partial \phi \partial V) \sin \alpha}{mV} - \frac{(\partial T / \partial \phi) \sin \alpha}{mV^2} \\ 0 \\ 0 \\ \frac{(\partial T / \partial \phi) \cos \alpha}{mV} \\ 0 \\ \frac{(\partial^2 T / \partial \phi^2) \sin \alpha}{mV} \\ 0 \end{bmatrix},$$

$$\omega_{25} = \omega_{27} = 0.$$

$$\mathbf{F}^*(\mathbf{x}) = \begin{bmatrix} F_1^*(\mathbf{x}) \\ F_2^*(\mathbf{x}) \end{bmatrix}, \tag{A5}$$

where

$$F_1^*(\mathbf{x}) = \omega_1 \ddot{\mathbf{x}}_0 + \dot{\mathbf{x}}^T \mathbf{\Omega}_1 \dot{\mathbf{x}},$$

$$F_2^*(\mathbf{x}) = 3\ddot{V} \dot{\gamma} \cos \gamma - 3\dot{V} \dot{\gamma}^2 \sin \gamma + 3\dot{V} \ddot{\gamma} \cos \gamma - 3V \dot{\gamma} \ddot{\gamma} \sin \gamma - V \dot{\gamma}^3 \cos \gamma$$

$$+ (\omega_1 \ddot{\mathbf{x}}_0 + \dot{\mathbf{x}}^T \mathbf{\Omega}_1 \dot{\mathbf{x}}) \sin \gamma + V (\omega_2 \ddot{\mathbf{x}}_0 + \dot{\mathbf{x}}^T \mathbf{\Omega}_2 \dot{\mathbf{x}}) \cos \gamma.$$

$$\mathbf{G}^*(\mathbf{x}) = \begin{bmatrix} \frac{\omega_n^2}{m} \cos \alpha & \frac{c_e \rho V^2 S \bar{c}}{2mI_y} \left(T \sin \alpha + \frac{\partial D}{\partial \alpha} \right) \\ \frac{(\partial T / \partial \phi) \omega_n^2}{m} \cos(\alpha + \gamma) & \frac{c_e \rho V^2 S \bar{c}}{2mI_y} \left(T \sin(\alpha + \gamma) + \frac{\partial L}{\partial \alpha} \cos \gamma - \frac{\partial D}{\partial \alpha} \sin \gamma \right) \end{bmatrix}. \tag{A6}$$